

## Role of the Fast Kinetics of Pyroglutamate-Modified Amyloid- $\beta$ Oligomers in Membrane Binding and Membrane Permeability

Joon Lee,<sup>‡</sup> Alan L. Gillman,<sup>†</sup> Hyunbum Jang,<sup>§</sup> Srinivasan Ramachandran,<sup>‡,†</sup> Bruce L. Kagan,<sup>||</sup> Ruth Nussinov,<sup>§,⊥</sup> and Fernando Teran Arce\*,<sup>‡,†</sup>

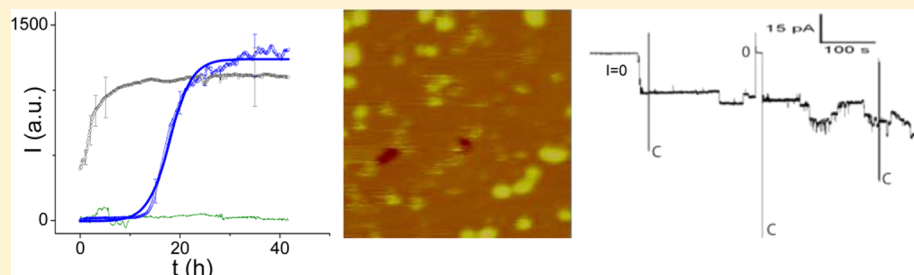
<sup>†</sup>Department of Bioengineering, University of California at San Diego, La Jolla, California 92093, United States

<sup>‡</sup>Department of Mechanical and Aerospace Engineering and Material Science Program, University of California at San Diego, La Jolla, California 92093, United States

<sup>§</sup>Cancer and Inflammation Program, National Cancer Institute at Frederick, Leidos Biomedical Research, Inc., Frederick National Laboratory for Cancer Research, Frederick, Maryland 21702, United States

<sup>||</sup>Department of Psychiatry, David Geffen School of Medicine, Semel Institute for Neuroscience and Human Behavior, University of California, Los Angeles, California 90024, United States

\*Department of Human Molecular Genetics and Biochemistry, Sackler School of Medicine, Tel Aviv University, Tel Aviv 69978, Israel



**ABSTRACT:** Membrane permeability to ions and small molecules is believed to be a critical step in the pathology of Alzheimer's disease (AD). Interactions of oligomers formed by amyloid- $\beta$  ( $A\beta$ ) peptides with the plasma cell membrane are believed to play a fundamental role in the processes leading to membrane permeability. Among the family of  $A\beta$ s, pyroglutamate (pE)-modified  $A\beta$  peptides constitute the most abundant oligomeric species in the brains of AD patients. Although membrane permeability mechanisms have been studied for full-length  $A\beta_{1-40/42}$  peptides, these have not been sufficiently characterized for the more abundant  $A\beta_{pE3-42}$  fragment. Here we have compared the adsorbed and membrane-inserted oligomeric species of  $A\beta_{pE3-42}$  and  $A\beta_{1-42}$  peptides. We find lower concentrations and larger dimensions for both species of membrane-associated  $A\beta_{pE3-42}$  oligomers. The larger dimensions are attributed to the faster self-assembly kinetics of  $A\beta_{pE3-42}$ , and the lower concentrations are attributed to weaker interactions with zwitterionic lipid headgroups. While adsorbed oligomers produced little or no significant membrane structural damage, increased membrane permeabilization to ionic species is understood in terms of enlarged membrane-inserted oligomers. Membrane-inserted  $A\beta_{pE3-42}$  oligomers were also found to modify the mechanical properties of the membrane. Taken together, our results suggest that membrane-inserted oligomers are the primary species responsible for membrane permeability.

**A**myloid- $\beta$  ( $A\beta$ ) peptides play a fundamental role in Alzheimer's disease (AD).<sup>1,2</sup> They are formed by enzymatic cleavage of the amyloid precursor protein (APP).<sup>3</sup> Although amyloid fibrils were originally believed to be the cytotoxic species in AD,<sup>4</sup> the emphasis has shifted toward smaller oligomers,<sup>5–15</sup> and a growing body of evidence indicates that intermediate  $A\beta$  oligomers are the toxic species while fibrils appear not to be involved in cytotoxicity.<sup>16–21</sup> Among the family of  $A\beta$  peptides, oligomers composed of pyroglutamate (pE)-modified  $A\beta$ s appear to be intimately involved in AD,<sup>18,22–24</sup> as they constitute the most abundant oligomeric species in the brains of AD patients, but their amount is significantly smaller in brains of age-matched individuals with normal cognition.<sup>18,22–24</sup> One of the most

abundant species, the  $A\beta_{pE3-42}$  fragment, is generated by cleavage of the first two amino acids at the N-terminus of  $A\beta_{1-42}$ , leaving a glutamate (E) residue in position 3. The pyroglutamate (pE) residue is subsequently generated by intramolecular dehydration.<sup>18,24</sup>

Self-assembly of  $A\beta$  peptides into polymorphic structures and their binding to lipid membranes are key processes in the pathogenesis of AD.<sup>17,25–28</sup> Although the exact molecular mechanisms of cell dysfunction are insufficiently understood,

Received: May 16, 2014

Revised: June 19, 2014

Published: June 20, 2014

they involve the interaction of oligomeric species with the plasma cell membrane.<sup>17,25,26,29–31</sup> Depending on lipid composition, membranes can promote the conformational changes of  $\text{A}\beta$ s that lead to the formation of toxic  $\beta$ -sheet structures and serve as nucleation sites for faster self-assembly. In addition, ganglioside-containing membranes have been found to play a role in altering the aggregation pathways of  $\text{A}\beta$ .<sup>32</sup> On the other hand,  $\text{A}\beta$  oligomers can induce permeabilization of the membrane to unregulated passage of small molecules and ions.<sup>2,17,26,33,34</sup> Potential mechanisms of membrane permeabilization include carpeting, pore formation, and the detergent effect.<sup>17,33–36</sup> Also, recent solid state nuclear magnetic resonance (NMR) studies of  $\text{A}\beta$  and the islet amyloid polypeptide (IAPP) peptides have shown similarities between the modes of membrane permeabilization of these amyloid peptides and those of the better studied antimicrobial peptides (AMPs).<sup>37,38</sup> Permeabilization mechanisms appear not to be mutually exclusive; for instance, pore formation appears to occur prior to membrane fragmentation.<sup>39</sup> All permeabilization mechanisms ultimately lead to changes in the cellular ionic concentration, producing a loss of cell homeostasis and subsequent cell death. These processes have been characterized for full-length  $\text{A}\beta_{1–40/42}$ , but similar studies are missing for the  $\text{A}\beta_{\text{pE}3–42}$  fragment.

$\text{A}\beta_{\text{pE}3–42}$  is more hydrophobic than  $\text{A}\beta_{1–42}$  because of the loss of negative charges from residues Asp1 and Glu3 and the formation of the lactam ring in the pE residue. This increased hydrophobicity affects the kinetics of self-assembly, as well as the interactions of the peptide with the membrane lipids. Here, we examine different mechanisms of membrane permeability induced by  $\text{A}\beta_{\text{pE}3–42}$  peptides. We compare the kinetics of self-assembly for  $\text{A}\beta_{\text{pE}3–42}$  and  $\text{A}\beta_{1–42}$  and examine the relationship between self-assembly and membrane binding. We used a mixture of phosphoethanolamine (PE) and phosphoserine (PS) lipid headgroups because these are dominant lipid components in the brains of the elderly,<sup>40</sup> and these levels have been found to change in AD brains.<sup>41</sup> We find lower concentrations of  $\text{A}\beta_{\text{pE}3–42}$  oligomers adsorbed on membrane surfaces, likely reflecting the weaker interactions between the more hydrophobic  $\text{A}\beta_{\text{pE}3–42}$  peptides and the lipid heads. The faster kinetics of  $\text{A}\beta_{\text{pE}3–42}$  self-assembly leads to larger dimensions of the adsorbed  $\text{A}\beta_{\text{pE}3–42}$  oligomers. These adsorbed oligomers produced little or no significant damage to the membrane. Membrane permeabilization to ionic species was observed as pore activity and can be understood as a result of oligomers inserted into the membrane.

## MATERIALS AND METHODS

**Peptide Handling.** Both  $\text{A}\beta_{1–42}$  and  $\text{A}\beta_{\text{pE}3–42}$ , >90% purity as provided by the manufacturer (Bachem, Torrance, CA), were first dissolved in 1% ammonium hydroxide until the peptides were completely dissolved. They were subsequently sonicated for approximately 2 min. The desired amount of peptide was aliquoted and lyophilized using a lyophilizer (FreeZone 2.5 Plus, Labconco, Kansas City, KS). The aliquots were stored at –80 °C for a maximum of 3 months until they were used. For every experiment, aliquoted peptides were taken from –80 °C and hydrated in Tris (pH 7.4) or HEPES (pH 7.0) buffer solutions. The peptide concentration was measured using the 280 nm UV absorbance (extinction coefficient:  $\epsilon = 1490 \text{ M}^{-1} \text{ cm}^{-1}$ ).

**Thioflavin-T (ThT) Assays.** A stock solution of 500  $\mu\text{M}$  ThT in water was prepared, and 2  $\mu\text{L}$  was added to 100  $\mu\text{L}$  of

10 mM HEPES [20 mM MgCl<sub>2</sub> and 150 mM NaCl (pH 7.0)] buffer in 96-well black-walled plates (Nunc) to make 10  $\mu\text{M}$  ThT solutions. For peptides, 20 mM NaOH was used to dissolve lyophilized aliquot peptides and prevent aggregation. After that, the peptide solution was diluted with HEPES to its final peptide concentration in the plate well, and the NaOH content was maintained at <10% of the total volume. ThT fluorescence (450 nm excitation, 490 nm emission) was monitored every 5 min at 25 °C for the indicated times using a SPECTRAmax Gemini EM fluorescent plate reader (Molecular Devices, Sunnyvale, CA). The obtained curves were fit using the sigmoidal curve in eq 1<sup>42</sup>

$$F = F_0 + \frac{a}{1 + e^{-k(t-t_{1/2})}} \quad (1)$$

where  $t$  is the time,  $t_{1/2}$  is the time to reach half-maximal ThT fluorescence,  $F_0$  is the initial fluorescence intensity,  $a$  is the amplitude of the maximal intensity, and  $k$  is the rate constant. The lag phase time was calculated from the fitting parameters obtained above using

$$t_{\text{lag}} = t_{1/2} - \frac{2}{k} \quad (2)$$

**Lipid Bilayer Preparation for Atomic Force Microscopy (AFM) Experiments.** For liposome preparation, 1-palmitoyl-2-oleoyl-sn-glycero-3-phosphoethanolamine (POPE) and 1,2-dioleoyl-sn-glycero-3-phospho-L-serine (DOPS) lipids were used in a 1:1 ratio (both purchased from Avanti Polar Lipids, Alabaster, AL). Liposomes were prepared by mixing 20  $\mu\text{L}$  of each lipid (5 mg/mL) dissolved in chloroform and allowed to dry overnight in vacuum. The dried lipid film was hydrated with a peptide solution to facilitate incorporation of the peptide in the lipid bilayer, resulting in proteoliposome formation. For imaging, peptide:lipid ratios in the range of 1:10 to 1:2 were used, while the peptide:lipid ratios for force mapping were 1:10. For the preparation of control liposomes, 200  $\mu\text{L}$  of 25 mM Tris buffer [300 mM NaCl (pH 7.4)] were used. The resulting liposome and proteoliposome suspensions were vortexed occasionally for approximately 1 h for better hydration. The large multilamellar vesicles formed with this procedure were sonicated for 5 min. These suspensions were subsequently extruded using 100 nm filters to produce small unilamellar vesicles. Supported lipid bilayers were formed by (proteo)liposome rupture and fusion on the mica substrate.<sup>43–45</sup> Lipid concentrations of 0.1–1 mg/mL were deposited on freshly cleaved mica and incubated for ~10 min on a hot plate above the lipid transition temperature to facilitate fusion of the ruptured proteoliposomes on the mica surface. As a last step, samples were rinsed with buffer to remove unruptured proteoliposomes still in solution. For incubation of  $\text{A}\beta_{\text{pE}3–42}$  on preformed lipid bilayer experiments, liposomes were allowed to form supported lipid bilayers on mica. The formation of bilayer patches was verified by AFM before incubation in peptide solutions.  $\text{A}\beta_{\text{pE}3–42}$  was injected in a buffer solution at the final concentration of 20  $\mu\text{M}$  for a given time at room temperature.

**AFM Imaging.** Topographic images were acquired using a Multimode atomic force microscope equipped with a Nanoscope V controller (Bruker, Santa Barbara, CA). Silicon cantilevers with a spring constant of 48 N/m (NSC11, JPK) were used for imaging in air using tapping mode. Silicon nitride cantilevers with spring constants of 0.08 N/m (OMCL-TR400, Olympus) were employed for imaging in fluid using tapping

mode. Resonance frequencies of  $\sim 8$  kHz and drive amplitudes under 100 mV were used. The Nanoscope software was used for analyzing imaging data. Particle analysis was used to measure the number of membrane-associated oligomers. Section analysis was used for measuring widths and heights of membrane-associated oligomers. Oligomer widths were measured as full widths at half the maximal height (fwhm) in section profiles, and these values were corrected to take tip widening effects into account. On the basis of previous models,<sup>43,46,47</sup> tip widening of the inserted oligomers was modeled as a spherical tip of radius  $R$  in contact with a spherical cap of radius  $r$  protruding a height  $h$  above the surface of the lipid bilayer (eqs 3 and 4).

$$D = 2\sqrt{rh - \frac{h^2}{4}} \quad (3)$$

$$r = \frac{x^2 - 2Rh + h^2}{2h} \quad (4)$$

where  $D$  is the corrected oligomer diameter and  $w = 2x$  is the measured width at half-height. Similarly, tip widening of the adsorbed oligomers was modeled as a spherical tip of radius  $R$  in contact with another sphere of radius  $r$  located on a surface.

$$y = r - R + \sqrt{(R + r)^2 - x^2} \quad (5)$$

where  $y$  is the height of the tip above the surface and  $w = 2x$  is the measured width at height  $y$ . Because widths were measured at half the measured oligomer height, we set  $y$  equal to  $r$ . Origin software (OriginLab Corp., Northampton, MA) was used to generate histograms and fitting curves in this section and all others.

**AFM Force Mapping.** For force mapping experiments, the atomic force microscope was changed to force volume mode after imaging an area of interest. Forces of  $<12$  nN and tip velocities of 800 nm/s were used. Force curves were acquired point by point in each point of a  $32 \times 32$  array (force map). Data processing for force mapping data was conducted by using a custom-made MATLAB (Natick, MA) program. Breakthrough forces were measured with this program by detecting the force discontinuity during a breakthrough event. When no event was detected, the breakthrough force was set to zero and no further analysis was performed on that curve. Statistical distributions of breakthrough forces were fit with Gaussian functions. All experiments were performed at room temperature. Actual spring constants were measured using the thermal tune method before the experiments.<sup>48</sup>

**Planar Lipid Bilayer Electrical Recording.** For electrical recording experiments with planar lipid bilayers (known as BLM for black lipid membranes because they appear "black" when viewed by reflected light),<sup>49,50</sup>  $A\beta_{pE3-42}$  peptides were dissolved in Milli-Q water to a concentration of 1 mg/mL and subsequently used a single time. Membranes were composed of DOPS/POPE mixtures (1:1 by weight) in heptane at a total lipid concentration of 20 mg/mL. For membrane formation, lipid was added directly over a hole ( $\sim 250$   $\mu$ m diameter) in a Delrin septum (Warner Instruments, Delrin perfusion cup, volume of 1 mL). As an electrolyte, we used 150 mM KCl, 10 mM HEPES (pH 7.4), and 1 mM MgCl<sub>2</sub>. Before data were acquired, we verified that the bilayer was stable for several minutes with a low conductance ( $<10$  pS) across an applied voltage of  $\pm 100$  mV and that the system capacitance was  $>110$  pF. When both criteria were met, the peptide solution was

added to one of the compartments of the bilayer chamber (*cis* side), reaching a final concentration of  $\sim 10$   $\mu$ M. The solution was stirred for 5 min before data were acquired. Bilayer stability was monitored by periodic capacitance measurements. All traces were recorded in voltage clamp mode using the 2 kHz built-in filter cutoff of our BC-535 amplifier (Warner Instruments, Hamden, CT). A sampling frequency of 15 kHz was used for the acquisition of data. We used a custom-made LabVIEW (National Instruments, Austin, TX) program to record the current and Clampfit version 10.2 (Molecular Devices) to analyze traces. For the representation in figures, time traces were filtered with a digital Gaussian low-pass filter with a cutoff frequency of 50 Hz.

## RESULTS

**Kinetics of  $A\beta_{pE3-42}$  Self-Assembly in Solution.** The ThT fluorescence was used to compare the kinetics of fibril self-

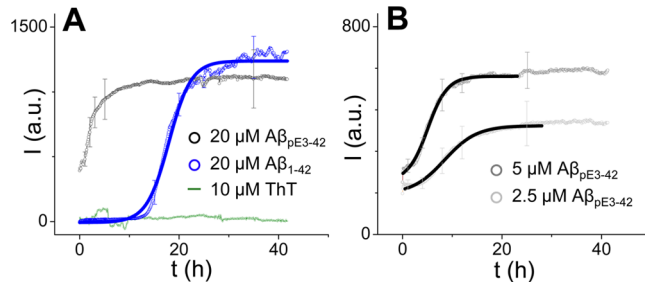


**Figure 1.** Self-assembly kinetics of  $A\beta_{1-42}$  and  $A\beta_{pE3-42}$  measured by thioflavin-T (ThT) fluorescence at 25 °C. The ThT intensity ( $I$ ) was monitored as a function of time ( $t$ ) for (A)  $A\beta_{pE3-42}$  (black) and  $A\beta_{1-42}$  (blue) solutions (fitted curve shown with a solid blue line) with 20  $\mu$ M concentrations (a.u., arbitrary units) and (B) 5  $\mu$ M (dark gray) and 2.5  $\mu$ M (light gray) solutions of  $A\beta_{pE3-42}$ . Fitted curves are shown with black lines.  $t_{lag}$  and  $k$  were obtained from the fitted curves using eqs 1 and 2.

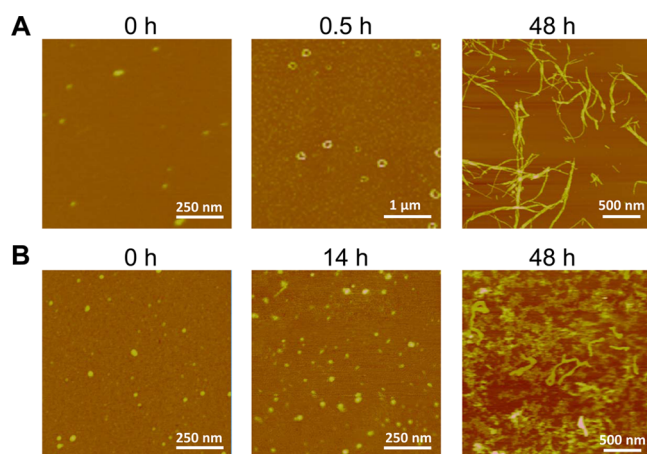


**Figure 2.** AFM images of (A)  $A\beta_{pE3-42}$  and (B)  $A\beta_{1-42}$  aggregated peptides after different periods of incubation. Images were acquired in air. A 10  $\mu$ L droplet was deposited on a mica surface for 5 min, rinsed with  $\sim 50$   $\mu$ L pure water and dried with gentle N<sub>2</sub> flow. The vertical color-coded scale is 10 nm everywhere except for the 48 h images, where it is 50 nm.

assembly for  $A\beta_{1-42}$  and  $A\beta_{pE3-42}$  peptides (Figure 1).  $A\beta_{pE3-42}$  peptides have faster self-assembly kinetics, indicated by a considerably shorter lag phase and a faster elongation phase

**Table 1. Heights ( $h$ ), Widths ( $W$ ), and Diameters ( $D$ ) for the Globular and Annular Oligomers of  $\text{A}\beta_{1-42}$  and  $\text{A}\beta_{\text{pE3-42}}$  Shown in Figure 2 at the Indicated Times ( $n = 28$  for all entries)<sup>a</sup>**

	$\text{A}\beta_{1-42}$ ( $t = 0$ ) <sup>b</sup>	$\text{A}\beta_{\text{pE3-42}}$ ( $t = 0$ ) <sup>b</sup>	$\text{A}\beta_{1-42}$ ( $t = 14$ h) <sup>b</sup>	$\text{A}\beta_{\text{pE3-42}}$ ( $t = 0.5$ h) <sup>b</sup>
$h$ (nm)	$1.7 \pm 0.7$	$1.1 \pm 0.6$	$3.9 \pm 1.6$	$2.3 \pm 0.9$
$W$ (nm)	$18.3 \pm 4.4$	$22.1 \pm 6.4$	$19.0 \pm 4.4$	$136.4 \pm 33.8^c$
$D$ (nm)	$7.3 \pm 3.1$	$10.1 \pm 5.0$	$7.7 \pm 3.1$	$136.4 \pm 33.8^c$

<sup>a</sup>The tip widening effect was considered for  $D$  using eq 5. <sup>b</sup>Values are presented as averages  $\pm$  the standard deviation. <sup>c</sup>The peak–peak distance (not affected by tip widening) was measured.

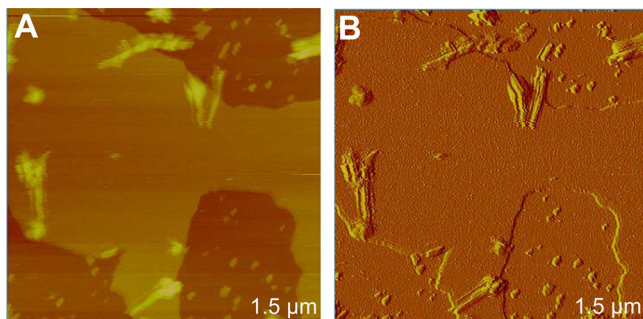


**Figure 3.** AFM (A) height and (B) amplitude images of  $\text{A}\beta_{\text{pE3-42}}$  fibrils formed on a supported DOPS/POPE (1:1) lipid membrane after incubation for 38 h at room temperature. Fibril structures on a seemingly intact membrane are observed. The vertical color-coded scale is 25 nm for panel A.

(Figure 1A). The lag phase for  $\text{A}\beta_{\text{pE3-42}}$  becomes visible only at the lower concentrations (Figure 1B). Their lag phase times and rate constants using eqs 1 and 2 are as follows:  $t_{\text{lag}} = 1.14$  h and  $k = 0.51 \text{ h}^{-1}$  for the 5  $\mu\text{M}$  solution, and  $t_{\text{lag}} = 2.01$  h and  $k = 0.31 \text{ h}^{-1}$  for the 2.5  $\mu\text{M}$  solution. From the fitted curves in

Figure 1A, we obtained a  $t_{\text{lag}}$  of 13.51 h and a  $k$  of  $0.46 \text{ h}^{-1}$  for  $\text{A}\beta_{1-42}$ . Our results are in good agreement with previous results for  $\text{A}\beta_{1-40}$  and  $\text{A}\beta_{\text{pE3-40}}$ ,<sup>51</sup> although those lag phase times are considerably longer. This is possibly due to the two additional hydrophobic residues (Ile41 and Ala42) at the C-terminus of the  $\text{A}\beta_{1-42}$  and  $\text{A}\beta_{\text{pE3-42}}$  peptides.

AFM was used to characterize the morphology of the self-assembled species. Only globular and small linear oligomers were seen in the initial state of the freshly prepared  $\text{A}\beta_{\text{pE3-42}}$  and  $\text{A}\beta_{1-42}$  oligomers (Figure 2). While annular  $\text{A}\beta_{\text{pE3-42}}$  protofibrils were already seen after incubation for 30 min at room temperature (Figure 2A), globular  $\text{A}\beta_{1-42}$  oligomers were still found even after incubation for 14 h (Figure 2B). The diameters of  $\text{A}\beta_{\text{pE3-42}}$  oligomers changed significantly after 0.5 h, whereas the diameters of  $\text{A}\beta_{1-42}$  oligomers remained approximately constant after 14 h (Table 1). The heights changed by a factor of  $\sim 2$  for both peptides (Table 1). As regions with high concentrations of  $\text{A}\beta_{\text{pE3-42}}$  fibrils were already seen after 48 h (Figure 2A), only protofibrils and large quantities of  $\text{A}\beta_{1-42}$  oligomers were observed (Figure 2B).  $\text{A}\beta_{1-42}$  fibrils were found only after incubation for several days. These results correlate well with the ThT data discussed above (Figure 1A).

**Membrane-Adsorbed  $\text{A}\beta_{\text{pE3-42}}$  Oligomers.** We used AFM to characterize the morphology of  $\text{A}\beta$  oligomers adsorbed on anionic membranes and the loss of membrane integrity induced by these oligomers. We attempted to monitor the adsorption of  $\text{A}\beta_{\text{pE3-42}}$  oligomers when they were allowed to interact with preformed supported lipid bilayers. We did not observe oligomer adsorption even after incubation for several hours in the AFM liquid cell. Instead, fibrils were observed on membrane regions after *ex situ* incubation for 38 h (Figure 3). Significantly, membrane patches appeared to be intact without a substantial number of adsorbed  $\text{A}\beta_{\text{pE3-42}}$  oligomers or apparent defects in the lipid bilayer. These results suggest

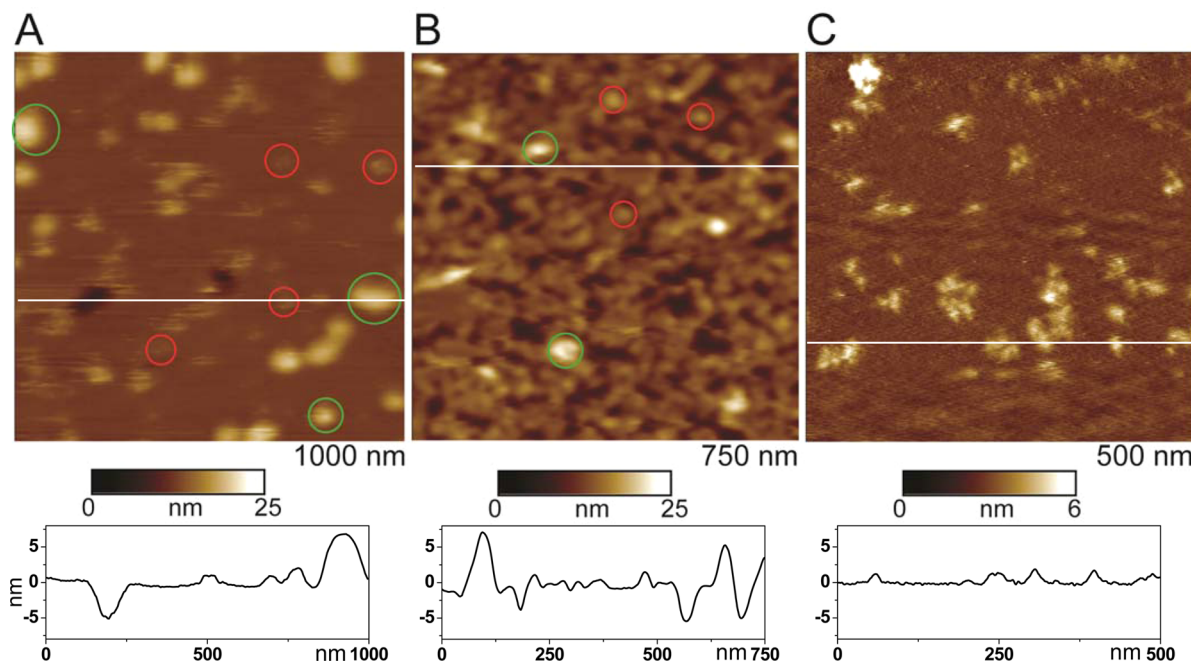


**Figure 4.** AFM images of (A)  $\text{A}\beta_{\text{pE3-42}}$  oligomers and membrane defects induced by the oligomers in a DOPS/POPE (1:1) lipid bilayer and (B)  $\text{A}\beta_{1-42}$  oligomers adsorbed on a lipid bilayer with the same composition described above. (C)  $\text{A}\beta_{1-42}$  oligomers adsorbed on a lipid bilayer with a lower peptide:lipid mass ratio. The peptide:lipid mass ratios are 1:2 in panels A and B and 1:10 in panel C.

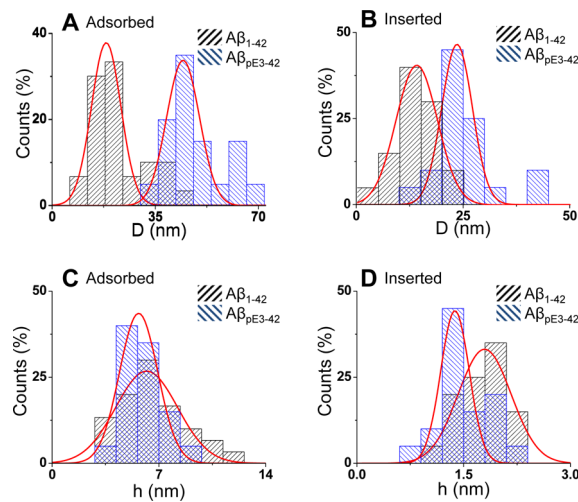


**Figure 5.** Diameter and height histograms of inserted and adsorbed oligomers obtained from AFM images similar to Figure 4. (A) Diameter ( $D$ ) histograms for membrane-adsorbed oligomers of  $A\beta_{pE3-42}$  (blue) and  $A\beta_{1-42}$  (black).  $A\beta_{pE3-42}$  oligomers have a diameter  $D_A(A\beta_{pE3-42})$  of  $43.8 \pm 7.6$  nm, while  $D_A(A\beta_{1-42}) = 21.5 \pm 7.6$  nm for  $A\beta_{1-42}$  oligomers. (B) Diameter histograms for inserted oligomers. Inserted  $A\beta_{pE3-42}$  oligomers (blue) have a diameter  $D_I(A\beta_{pE3-42})$  of  $26.0 \pm 7.1$  nm, whereas  $D_I(A\beta_{1-42}) = 13.8 \pm 4.8$  nm for  $A\beta_{1-42}$  oligomers (black). Diameters were measured as described in the Methods section. (C) Height ( $h$ ) histograms for membrane-adsorbed oligomers of  $A\beta_{pE3-42}$  (blue) and  $A\beta_{1-42}$  (black).  $A\beta_{pE3-42}$  oligomers have a height  $h_A(A\beta_{pE3-42})$  of  $5.7 \pm 1.5$  nm, while  $h_A(A\beta_{1-42}) = 6.2 \pm 2.4$  nm for  $A\beta_{1-42}$  oligomers. (D) Height histograms for inserted oligomers of  $A\beta_{pE3-42}$  (blue) and  $A\beta_{1-42}$  (black).  $A\beta_{pE3-42}$  oligomers have a height  $h_I(A\beta_{pE3-42})$  of  $1.4 \pm 0.2$  nm, while  $h_I(A\beta_{1-42}) = 1.8 \pm 0.4$  nm for  $A\beta_{1-42}$  oligomers. Histograms were fit using a Gaussian function, and  $D$  and  $h$  values are given as peak center values  $\pm$  the half-width at half-maximum of the distribution. A height of 2 nm was chosen as the boundary between inserted and adsorbed species.  $n = 20$  for all histograms, except  $n = 30$  for  $D_I(A\beta_{1-42})$  and  $h_I(A\beta_{1-42})$ .

weak interactions between  $A\beta_{pE3-42}$  oligomers and headgroups in the lipid membrane. In comparison, oligomeric and fibrillar self-assembled structures of full-length  $A\beta$ s were found to form on different supported membranes.<sup>52–56</sup>

To increase the probability of  $A\beta$  peptides interacting with membrane lipids, lipids were hydrated into liposomes in the presence of peptides, subsequently sonicated together, and finally extruded to form unilamellar proteoliposomes. Following this method, large quantities of  $A\beta_{pE3-42}$  oligomers adsorbed on a seemingly flat membrane were seen (Figure 4A). The adsorbed  $A\beta_{pE3-42}$  oligomers (green circles) have typical diameters in the range of 30–40 nm and heights of 2–10 nm (Figures 4A and 5A,C and Table 2). In addition, bilayer deep (~5 nm) gaps separating regions of seemingly intact patches are observed. Smaller structures ( $\leq 2$  nm in height) are

found in these flatter regions, suggesting the presence of membrane-inserted oligomers. We compared the density and dimensions of adsorbed  $A\beta_{pE3-42}$  oligomers with those of  $A\beta_{1-42}$  oligomers. The  $A\beta_{1-42}$  oligomers have higher concentrations ( $\sim 200$  oligomers/ $\mu\text{m}^2$ ) and smaller dimensions compared to those of the  $A\beta_{pE3-42}$  oligomers even though their heights are similar (Figures 4B and 5A,C and Table 2). In addition, a large surface density of membrane defects with depths of one bilayer (dark spots) is observed. At lower peptide:lipid ratios (Figure 4C), the number of these defects was no longer significant and most of the observed structures protruded  $\leq 2$  nm from the bilayer plane, suggesting a majority of inserted oligomers.

**Membrane-Inserted  $A\beta_{pE3-42}$  Oligomers.** In addition to the adsorbed oligomers discussed above, we observed numerous smaller structures protruding  $< 2$  nm from the membrane plane (red circles in Figures 4A,B). These structures are attributed to populations of oligomers inserted into the membrane. Similar to the membrane-adsorbed oligomers, the inserted  $A\beta_{1-42}$  oligomers have higher concentrations and smaller dimensions compared to those of the  $A\beta_{pE3-42}$  oligomers (Figures 4A,B and 5B,D and Table 2). Most of these oligomers have a globular appearance (Figure 6A), although a smaller subpopulation of pore-forming oligomers was also found (inset). Their electrophysiological activity is indicated by discrete features in the ionic current passing through the lipid membrane (Figure 6B), with pore conductances of  $< 0.7$  nS.<sup>57</sup> From these data, the pore diameters can be roughly approximated (Figure 6C) using eq 6:<sup>58,59</sup>

$$r = r_0 \left[ 1 + \left( 1 + \frac{4L}{\pi r_0} \right)^{1/2} \right] \quad (6)$$

with  $r$  is the pore radius,  $r_0 = G/4\sigma$ ,  $G$  is the single-pore conductance,  $\sigma$  is the solution conductivity ( $\sim 1.5$  S/m for 150 mM KCl), and  $L$  is the pore length ( $\sim 6$  nm). After longer recording times ( $\sim 20$  min following the first activity) and in approximately 50% of our experiments, an exponential-like phase was observed before the saturation current of the amplifier was reached.<sup>57</sup>

We conducted force measurements on membrane patches with inserted  $A\beta_{pE3-42}$  oligomers. We characterized the mechanical properties of these membranes by measuring the breakthrough force seen in indentation curves. These curves show that lipid membranes are first deformed elastically by the AFM tip (O–F<sub>B</sub> region in Figure 7A). At the critical breakthrough force, marked by a discontinuity in the curve, the membrane undergoes an irreversible (plastic) deformation. The breakthrough force has been characterized for different lipid membranes and found to be sensitive to lipid composition, ionic strength, and temperature.<sup>60–69</sup> We measured a value of  $1.31 \pm 0.22$  nN (mean value  $\pm$  the half-width at half-

**Table 2. Densities ( $n_O$ ) of Membrane-Associated Oligomers (inserted and adsorbed) and Measured Widths, Diameters, and Heights of Inserted and Adsorbed  $A\beta_{1-42}$  and  $A\beta_{pE3-42}$  Oligomers ( $W_I$ ,  $D_I$ ,  $h_I$ ,  $W_A$ ,  $D_A$ , and  $h_A$ , respectively)<sup>a</sup>**

peptide	$n_O$ ( $\mu\text{m}^{-2}$ )	$W_I$ (nm) <sup>b</sup>	$W_A$ (nm) <sup>b</sup>	$D_I$ (nm) <sup>c</sup>	$D_A$ (nm) <sup>c</sup>	$h_I$ (nm) <sup>b</sup>	$h_A$ (nm) <sup>b</sup>
$A\beta_{pE3-42}$	43	$38.2 \pm 6.9$	$62.2 \pm 12.5$	$26.0 \pm 7.08$	$43.8 \pm 7.6$	$1.4 \pm 0.2$	$5.7 \pm 1.5$
$A\beta_{1-42}$	195	$22.7 \pm 6.7$	$33.5 \pm 5.7$	$13.8 \pm 4.77$	$21.5 \pm 7.6$	$1.8 \pm 0.4$	$6.2 \pm 2.4$

<sup>a</sup> $n_O$  was measured using particle analysis for all oligomers in panels A and B of Figure 4, while all other values were measured for individual oligomers;  $n = 20$  everywhere, except  $n = 30$  for  $D_I(A\beta_{1-42})$  and  $h_I(A\beta_{1-42})$ . <sup>b</sup>Values are represented as peak centers  $\pm$  the half-width at half-maximum from the Gaussian fitting. <sup>c</sup>Diameters were obtained from the measured widths by taking into account eqs 3–5 for tip deconvolution.

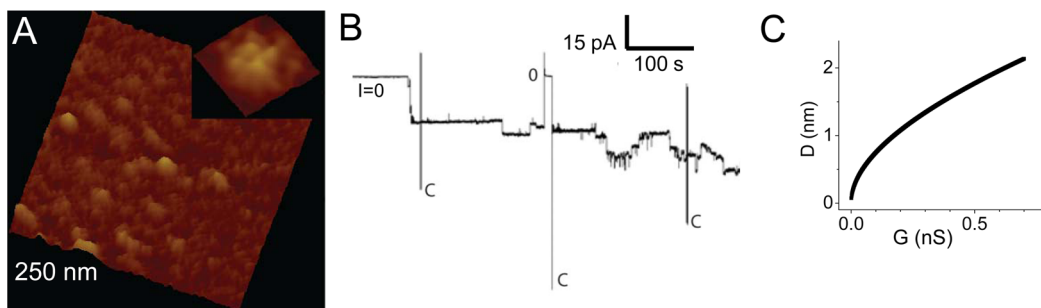


**Figure 6.** (A) AFM image of  $\text{A}\beta_{\text{pE3-42}}$  oligomers inserted into a DOPS/POPE (1:1) membrane. A subpopulation of these oligomers forms pore structures. (B) Electrical recording data demonstrating the activity induced by  $\text{A}\beta_{\text{pE3-42}}$  pore-forming oligomers. (C) Pore diameters estimated from eq 6 for the interval of single-pore conductances measured in our experiments (0–0.7 nS).

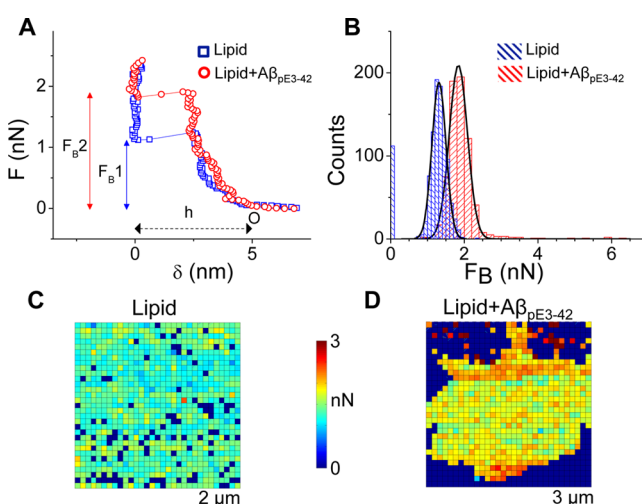


**Figure 7.** AFM force measurements demonstrating the effect of membrane-inserted  $\text{A}\beta_{\text{pE3-42}}$  oligomers on the mechanical properties of DOPS/POPE membranes. (A) Indentation curves (only approach is shown) for DOPS/POPE membranes without (blue) and with (red) inserted  $\text{A}\beta_{\text{pE3-42}}$  oligomers displaying the breakthrough forces ( $F_B$ ) and thicknesses ( $h$ ) of the membranes.  $F$  is the force, and  $\delta$  is the tip–sample separation. (B) Histograms of breakthrough forces show  $F_B1 = 1.31 \pm 0.19$  nN for the DOPS/POPE membrane and  $F_B2 = 1.83 \pm 0.25$  nN for a similar membrane with inserted  $\text{A}\beta_{\text{pE3-42}}$  oligomers. (C and D) Force maps of the analyzed data for (C) the DOPS/POPE membrane and (D) the DOPS/POPE membrane with inserted  $\text{A}\beta_{\text{pE3-42}}$  oligomers. The outline of the membrane patch is seen in panel D. An  $F_B$  value of 0 was given to curves that did not show breakthrough forces outside the membrane. These curves were not analyzed further. The peptide:lipid ratio is 1:10 for all data.

maximum) for the breakthrough force of DOPS/POPE membranes. Insertion of  $\text{A}\beta_{\text{pE3-42}}$  oligomers significantly increased this value by  $\sim 40\%$  (Figure 7B–D).

## DISCUSSION

Using ThT fluorescence, we have found that self-assembly of  $\text{A}\beta_{\text{pE3-42}}$  oligomers into fibrils has faster kinetics than that of  $\text{A}\beta_{1-42}$  (Figure 1). During the first phase, the lag phase, monomers and small oligomers nucleate with very slow kinetics into  $\beta$ -structured oligomers serving as nucleation seeds. In the second phase, these seeds elongate into amyloid fibrils at a much faster rate as more peptides are incorporated into the preformed seeds. Hydrophobic interactions and hydrogen bonding are the driving forces behind the self-assembly processes leading to amyloid fibril formation.<sup>70</sup> A recent  $^{19}\text{F}$

NMR study has reported multiple oligomeric species in the lag phase, including  $\alpha$ -helix and reversible  $\beta$ -sheet oligomers.<sup>71</sup> In addition, it has been reported that  $\text{A}\beta_{1-40}$  adopts a compact, partially folded structure, forming a  $3_{10}$ -helix in the H13–D23 central hydrophobic region,<sup>72</sup> and that these helical intermediates are crucial intermediates in amyloid self-assembly.

Annular protofibrils with polygonal appearances and diameters of 8–25 nm have been observed by transmission electron microscopy (TEM) for  $\text{A}\beta_{1-42}$  as a product of their aggregation process.<sup>73</sup> The diameters of the  $\text{A}\beta_{\text{pE3-42}}$  annular protofibrils we found (Figure 2A) are significantly larger, ranging from 80 to 200 nm (Table 1). The shapes we observed agree with the TEM observations for  $\text{A}\beta_{1-42}$ ; thus, they cannot be attributed to AFM imaging artifacts. Although annular protofibrils have been reported for many different amyloids,<sup>12,16,74,75</sup> their structures, interrelationships, and contributions to disease pathogenesis are not entirely clear.<sup>73</sup>

We have considered mechanisms of membrane permeability and loss of membrane structural integrity induced by  $\text{A}\beta_{\text{pE3-42}}$  oligomers (i) adsorbed on the membrane and (ii) inserted into the membrane. We observed a higher surface density of adsorbed  $\text{A}\beta_{\text{pE3-42}}$  oligomers when they were allowed to interact with lipids during lipid hydration and lipid self-assembly into liposomes (method 1) than when the oligomers were injected on preformed supported bilayers (method 2). This observation suggests that the former oligomers have a different, more favorable membrane-binding conformation than the latter. The additional energy necessary for oligomers to acquire this conformation might be provided during the sonication step in method 1. The higher fluidity of the liposome membrane might also facilitate rearrangement of the peptide in method 1, compared to the surface-supported membrane of method 2.

We found significantly larger dimensions and lower densities for membrane-adsorbed and membrane-inserted  $\text{A}\beta_{\text{pE3-42}}$  oligomers than for  $\text{A}\beta_{1-42}$  oligomers (Figures 4 and 5 and Table 2). The larger size of  $\text{A}\beta_{\text{pE3-42}}$  oligomers is attributed to their faster kinetics of self-assembly (Figures 1 and 2). The higher density of  $\text{A}\beta_{1-42}$  oligomers appears to be counter-intuitive because of the repulsion expected between the negatively charged Asp1 and Glu3 residues of  $\text{A}\beta_{1-42}$ , with the also negatively charged PS headgroups in the membrane. However, this higher density of  $\text{A}\beta_{1-42}$  oligomers is understandable if we hypothesize that PE-rich domains are induced by  $\text{A}\beta_{1-42}$  oligomers due to attractive charge–dipole interactions between the negatively charged residues and the zwitterionic PE headgroups (Figure 8), thus leading to formation of PE-rich proteoliposomes during lipid hydration

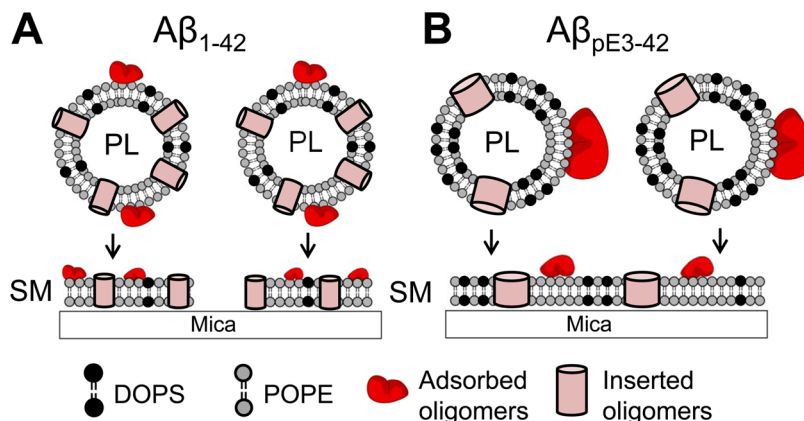


**Figure 8.** Schematics of supported membrane (SM) formation via proteoliposome (PL) rupture and fusion. (A)  $\text{A}\beta_{1-42}$  proteoliposomes having a very high concentration of membrane-inserted oligomers are not able to form supported membranes by fusion of ruptured proteoliposomes. (B)  $\text{A}\beta_{\text{pE}3-42}$  proteoliposomes have lower concentrations of inserted oligomers, thus being able to form supported membranes. The dimensions of the inserted and adsorbed  $\text{A}\beta_{\text{pE}3-42}$  oligomers are larger because of faster aggregation kinetics. Attractive interactions between  $\text{A}\beta_{1-42}$  and PE headgroups induce PE-rich proteoliposomes.

**Table 3. Comparison of Pore Diameters for  $\text{A}\beta_{\text{pE}3-42}$ ,  $\text{A}\beta_{1-42}$ , and  $\text{A}\beta_{17-42}$  Obtained from eq 6, MD Simulations, and AFM**

peptide	pore diameter (nm)	method
any	0.7–2.1	eq 6 for 100–700 pS
$\text{A}\beta_{\text{pE}3-42}$	~2.2 (18-mer, conformer 1)	MD <sup>57</sup>
	~1.9 (18-mer, conformer 2)	
$\text{A}\beta_{1-40}$	~1.0–2.0	AFM <sup>14</sup>
$\text{A}\beta_{1-42}$	~1.9 (18-mer, conformer 1, D-isomer)	MD <sup>43,78,90</sup>
	~2.1 (18-mer, conformer 2, D-isomer)	
	~1.8–2.2 (18-mer, conformer 1, L-isomer)	
	~1.9–2.2 (18-mer, conformer 2, L-isomer)	
	~1.0–2.0	AFM <sup>44</sup>
$\text{A}\beta_{17-42}$	~1.7 (16-mer channel)	MD <sup>44</sup>
	~0.8, ~1.9, ~2.5–2.7 (12-, 20-, and 24-mer channels)	MD <sup>91,92</sup>
	~1.8, ~1.5, ~2.2 (12-, 16-, and 20-mer barrels)	MD <sup>93</sup>

in our proteoliposome preparation protocol (method 1). In addition, the larger size of  $\text{A}\beta_{\text{pE}3-42}$  oligomers would increase the barrier for membrane insertion leading to lower densities of inserted  $\text{A}\beta_{\text{pE}3-42}$  oligomers. However, once the peptide is inserted, the stronger interactions of the more hydrophobic  $\text{A}\beta_{\text{pE}3-42}$  with the lipid tails would lead to a more stable conformation in the hydrophobic lipid core.

We interpret the high level of fragmentation of supported membranes formed from  $\text{A}\beta_{1-42}$  proteoliposomes (Figure 4B) to be due to insufficient vesicle fusion induced by the high concentration and steric repulsion of membrane-inserted  $\text{A}\beta_{1-42}$  oligomers (Figure 8). The larger dimensions of inserted and adsorbed  $\text{A}\beta_{\text{pE}3-42}$  oligomers (Figure 5 and Table 2) are attributed to their faster kinetics of self-assembly (Figures 1 and 2 and Table 1). We believe that even relatively low concentrations of  $\text{A}\beta_{\text{pE}3-42}$  oligomers can produce high cytotoxicity because of higher level of pore formation and higher stability in the membrane. Our BLM results indicating a larger populations of high-conductance  $\text{A}\beta_{\text{pE}3-42}$  pores as well as our molecular dynamics (MD) simulations indicating a more

stable membrane conformation of inserted  $\text{A}\beta_{\text{pE}3-42}$  pore structures lead to a similar conclusion.<sup>57</sup>

Among the populations of membrane-inserted oligomers, pore structures are observed less frequently than globular structures, suggesting that the former structures represent a minority population in the membrane. This is partly due to experimental difficulties in achieving a sufficiently high resolution by AFM, including the inability of broad tips to resolve pore features and the potential distortion of pore structures induced by tip–sample interactions. It should be noted, however, that even small pore populations have the ability to produce high cytotoxicity. It was estimated that a single pore with a 4 nS conductance would produce a loss of cell homeostasis in seconds.<sup>76,77</sup> A group of pores with the conductances observed in our data ( $\leq 0.7$  nS) would lead to a similar result.

Because of the different sensitivities between AFM imaging and BLM, higher pore concentrations are required for AFM imaging. For BLM, the opening of a single pore can produce a detectable increase in the current across the bilayer. As bilayer areas have typical dimensions of  $\sim 10^4 \mu\text{m}^2$ , pore densities of  $\sim 10^{-4}$  pores/ $\mu\text{m}^2$  can be detected by BLM. However, pore densities of  $\sim 10^2$ – $10^3$  pores/ $\mu\text{m}^2$  are necessary for optimal AFM imaging (1–10 pores for  $100 \text{ nm} \times 100 \text{ nm}$  imaging areas). Therefore, BLM provides information about early stages of pore formation when pore densities are low, while AFM gives information about later stages when the concentration of membrane-inserted oligomers is higher.

The pore diameters found using eq 6 (Figure 5C) are in general smaller than those predicted in MD simulations and seen by AFM imaging (Table 3). The relation in eq 6 assumes a cylindrical geometry with no charge along the length of the pore, while  $\text{A}\beta$  pores have a charged surface and a nonuniform geometry. As a result, the relation provides only a very rough estimate of pore diameter that is used as a “ballpark” figure. With this in mind, the calculated diameters compare reasonably well with the inner diameters of  $\text{A}\beta$  pores found using MD simulations and AFM imaging ( $\sim 1.5$ – $2.5$  nm). The structures of these membrane-embedded pores have been well characterized by AFM for full-length  $\text{A}\beta$ s,<sup>13,14,43</sup>  $\text{A}\beta_{1-42}$  point substitutions,<sup>78</sup>  $\text{A}\beta$  fragments,<sup>27,44</sup> and other amyloidogenic proteins.<sup>14,79</sup> Here, they were not investigated in detail. The

pore diameters for 18-mers of  $A\beta_{pE3-42}$  found using atomistic MD simulations were 1.9 and 2.2 nm for two different  $A\beta$  conformers.<sup>57</sup>

We measured a 40% increase in the breakthrough force of membranes allowed to interact with  $A\beta_{pE3-42}$  oligomers using method 1 of sample preparation. For these experiments, we used a 1:10 peptide:lipid ratio. At this ratio, we observed a sizable population of inserted  $A\beta_{pE3-42}$  oligomers (Figure 6), but not many adsorbed oligomers. In the presence of the latter population, the mechanical response measured by the tip likely would have been dominated by the adsorbed oligomers directly under the tip, not by their influence on the mechanical properties of the membrane. Therefore, our results indicate that the population of inserted oligomers induces a significant modification of the mechanical properties of the membrane.

The higher breakthrough force measured for membranes with inserted  $A\beta_{pE3-42}$  oligomers would suggest (i) the presence of local populations of rigid  $\beta$ -sheet oligomers, leading to increased local stiffness, or (ii) an increased global ordering of the membrane lipids induced by the  $A\beta_{pE3-42}$  oligomers, thus leading to a global increase in the stiffness of the membrane, similar to the modulation of membrane stiffness induced by cholesterol molecules.<sup>80–87</sup> From our measurements, we cannot discriminate which mechanism is predominant. Both stiffer and more flexible membranes could lead to higher membrane permeability, although by different mechanisms. A membrane hole would likely heal slower for stiffer membranes, thus enhancing permeability, and a more flexible hole would decrease the membrane thickness, also leading to increased permeability. Previous results found the breakthrough force of POPC/POPS membranes to increase when they were allowed to interact with  $A\beta_{1-40}$  oligomers and to be dependent on the aggregation state of the peptide.<sup>88</sup> Significantly,  $A\beta_{1-42}$  oligomers induced a decrease in the breakthrough force of supported membranes.<sup>89</sup> Some variability in the results is not surprising, as the free energy landscape of  $A\beta$ s has been found to be highly dependent on the exact experimental conditions.<sup>27,28,70</sup>

## CONCLUSIONS

We have examined the effect of  $A\beta_{pE3-42}$  oligomers on the ion permeability and the structural and mechanical properties of anionic lipid membranes. We have found lower concentrations and larger dimensions for the adsorbed and membrane-inserted  $A\beta_{pE3-42}$  oligomers compared to those of  $A\beta_{1-42}$ . The larger sizes of  $A\beta_{pE3-42}$  oligomers are attributed to their faster kinetics of self-assembly. The lower concentrations are attributed to their weaker interactions with the membrane lipids. However, once inserted into the membrane, these larger  $A\beta_{pE3-42}$  oligomers induce considerable ion permeability through the membrane and are stable in the lipid core of the membrane because of their increased hydrophobicity. The adsorbed  $A\beta_{pE3-42}$  oligomers appeared to have little effect on the structural integrity of the membrane. Membrane permeabilization can be understood more easily as a result of the membrane oligomers. These oligomers also produced a change in the mechanical properties of the membrane, suggesting a reordering of membrane structure.

## AUTHOR INFORMATION

### Corresponding Author

\*Departments of Bioengineering and Mechanical and Aerospace Engineering, University of California at San Diego

(UCSD), PFBH 218, 9500 Gilman Dr., MC 0412, La Jolla, CA 92093-0412. E-mail: ftarce@ucsd.edu. Telephone: (858) 822-1322.

### Funding

Support by the National Institutes of Health (R01AG028709) is acknowledged. A.L.G. was supported in part by National Institutes of Health Neuroplasticity of Aging Training Grant T32 AG 000216 and the Howard Hughes Medical Institute Med Into Grad Initiative. This project has been funded in whole or in part with Federal funds from the Frederick National Laboratory for Cancer Research, National Institutes of Health (NIH), under Contract HHSN261200800001E. This research was supported, in part, by the Intramural Research Program of the NIH, Frederick National Lab, Center for Cancer Research.

### Notes

The authors declare no competing financial interest.

## ACKNOWLEDGMENTS

We are deeply thankful to Prof. Ratnesh Lal for his insight and support for this work. All simulations had been performed using the high-performance computational facilities of the Biowulf PC/Linux cluster at the National Institutes of Health (Bethesda, MD).

## REFERENCES

- (1) Hardy, J. A., and Higgins, G. A. (1992) Alzheimer's Disease: The Amyloid Cascade Hypothesis. *Science* 256, 184–185.
- (2) DeToma, A. S., Salamekh, S., Ramamoorthy, A., and Lim, M. H. (2012) Misfolded proteins in Alzheimer's disease and type II diabetes. *Chem. Soc. Rev.* 41, 608–621.
- (3) Thinakaran, G., and Koo, E. H. (2008) Amyloid Precursor Protein Trafficking, Processing, and Function. *J. Biol. Chem.* 283, 29615–29619.
- (4) Sipe, J. D., and Cohen, A. S. (2000) Review: History of the amyloid fibril. *J. Struct. Biol.* 130, 88–98.
- (5) Bernstein, S. L., Dupuis, N. F., Lazo, N. D., Wyttenbach, T., Condron, M. M., Bitan, G., Teplow, D. B., Shea, J. E., Ruotolo, B. T., Robinson, C. V., and Bowers, M. T. (2009) Amyloid- $\beta$  protein oligomerization and the importance of tetramers and dodecamers in the aetiology of Alzheimer's disease. *Nat. Chem.* 1, 326–331.
- (6) Bernstein, S. L., Wyttenbach, T., Baumketner, A., Shea, J. E., Bitan, G., Teplow, D. B., and Bowers, M. T. (2005) Amyloid  $\beta$ -protein: Monomer structure and early aggregation states of  $A\beta$ 42 and its Pro(19) alloform. *J. Am. Chem. Soc.* 127, 2075–2084.
- (7) Chiti, F., and Dobson, C. M. (2006) Protein misfolding, functional amyloid, and human disease. *Annu. Rev. Biochem.* 75, 333–366.
- (8) Eisenberg, D., and Jucker, M. (2012) The Amyloid State of Proteins in Human Diseases. *Cell* 148, 1188–1203.
- (9) Glabe, C. G. (2008) Structural Classification of Toxic Amyloid Oligomers. *J. Biol. Chem.* 283, 29639–29643.
- (10) Jang, H., Zheng, J., Lal, R., and Nussinov, R. (2008) New structures help the modeling of toxic amyloid  $\beta$  ion channels. *Trends Biochem. Sci.* 33, 91–100.
- (11) Lashuel, H. A., Hartley, D., Petre, B. M., Walz, T., and Lansbury, P. T., Jr. (2002) Neurodegenerative disease: Amyloid pores from pathogenic mutations. *Nature* 418, 291.
- (12) Lashuel, H. A., and Lansbury, P. T., Jr. (2006) Are amyloid diseases caused by protein aggregates that mimic bacterial pore-forming toxins? *Q. Rev. Biophys.* 39, 167–201.
- (13) Lin, H. A. I., Bhatia, R., and Lal, R. (2001) Amyloid  $\beta$  protein forms ion channels: Implications for Alzheimer's disease pathophysiology. *FASEB J.* 15, 2433–2444.
- (14) Quist, A., Doudevski, I., Lin, H., Azimova, R., Ng, D., Frangione, B., Kagan, B., Ghiso, J., and Lal, R. (2005) Amyloid ion channels: A

- common structural link for protein-misfolding disease. *Proc. Natl. Acad. Sci. U.S.A.* 102, 10427–10432.
- (15) Kagan, B. L., Hirakura, Y., Azimov, R., Azimova, R., and Lin, M. C. (2002) The channel hypothesis of Alzheimer's disease: Current status. *Peptides* 23, 1311–1315.
- (16) Bucciantini, M., Giannoni, E., Chiti, F., Baroni, F., Formigli, L., Zurdo, J. S., Taddei, N., Ramponi, G., Dobson, C. M., and Stefani, M. (2002) Inherent toxicity of aggregates implies a common mechanism for protein misfolding diseases. *Nature* 416, 507–511.
- (17) Butterfield, S. M., and Lashuel, H. A. (2010) Amyloidogenic Protein–Membrane Interactions: Mechanistic Insight from Model Systems. *Angew. Chem., Int. Ed.* 49, 5628–5654.
- (18) Jawhar, S., Wirths, O., and Bayer, T. A. (2011) Pyroglutamate Amyloid- $\beta$  ( $A\beta$ ): A Hatchet Man in Alzheimer Disease. *J. Biol. Chem.* 286, 38825–38832.
- (19) Nussbaum, J. M., Schilling, S., Cynis, H., Silva, A., Swanson, E., Wangsanut, T., Tayler, K., Wiltgen, B., Hatami, A., Ronicke, R., Reymann, K., Hutter-Paier, B., Alexandru, A., Jagla, W., Graubner, S., Glabe, C. G., Demuth, H. U., and Bloom, G. S. (2012) Prion-like behaviour and tau-dependent cytotoxicity of pyroglutamylated amyloid- $\beta$ . *Nature* 485, 651–655.
- (20) Kirkitadze, M. D., Bitan, G., and Teplow, D. B. (2002) Paradigm shifts in Alzheimer's disease and other neurodegenerative disorders: The emerging role of oligomeric assemblies. *J. Neurosci. Res.* 69, 567–577.
- (21) Stroud, J. C., Liu, C., Teng, P. K., and Eisenberg, D. (2012) Toxic fibrillar oligomers of amyloid- $\beta$  have cross- $\beta$  structure. *Proc. Natl. Acad. Sci. U.S.A.* 109, 7717–7722.
- (22) Saido, T. C., YamaoHarigaya, W., Iwatsubo, T., and Kawashima, S. (1996) Amino- and carboxyl-terminal heterogeneity of  $\beta$ -amyloid peptides deposited in human brain. *Neurosci. Lett.* 215, 173–176.
- (23) Russo, C., Violani, E., Salis, S., Venezia, V., Dolcini, V., Damonte, G., Benatti, U., D'Arrigo, C., Patrone, E., Carlo, P., and Schettini, G. (2002) Pyroglutamate-modified amyloid  $\beta$ -peptides: A  $\beta$  N3(pE)-strongly affect cultured neuron and astrocyte survival. *J. Neurochem.* 82, 1480–1489.
- (24) Saido, T. C., Iwatsubo, T., Mann, D. M. A., Shimada, H., Ihara, Y., and Kawashima, S. (1995) Dominant and Differential Deposition of Distinct  $\beta$ -Amyloid Peptide Species,  $\alpha$ - $\beta$ (N3(pE)), in Senile Plaques. *Neuron* 14, 457–466.
- (25) Di Paolo, G., and Kim, T. W. (2011) Linking lipids to Alzheimer's disease: Cholesterol and beyond. *Nat. Rev. Neurosci.* 12, 284–296.
- (26) Relini, A., Cavalleri, O., Rolandi, R., and Gliozi, A. (2009) The two-fold aspect of the interplay of amyloidogenic proteins with lipid membranes. *Chem. Phys. Lipids* 158, 1–9.
- (27) Teran Arce, F., Jang, H., Ramachandran, S., Landon, P. B., Nussinov, R., and Lal, R. (2011) Polymorphism of amyloid  $\beta$  peptide in different environments: Implications for membrane insertion and pore formation. *Soft Matter* 7, 5267–5273.
- (28) Miller, Y., Ma, B., and Nussinov, R. (2010) Polymorphism in Alzheimer  $A\beta$  Amyloid Organization Reflects Conformational Selection in a Rugged Energy Landscape. *Chem. Rev.* 110, 4820–4838.
- (29) Jang, H., Connelly, L., Teran Arce, F., Ramachandran, S., Kagan, B. L., Lal, R., and Nussinov, R. (2013) Mechanisms for the Insertion of Toxic, Fibril-like  $\beta$ -Amyloid Oligomers into the Membrane. *J. Chem. Theory Comput.* 9, 822–833.
- (30) Matsuzaki, K., and Horikiri, C. (1999) Interactions of amyloid  $\beta$ -peptide (1–40) with ganglioside-containing membranes. *Biochemistry* 38, 4137–4142.
- (31) Matsuzaki, K., Kato, K., and Yanagisawa, K. (2010)  $A\beta$  polymerization through interaction with membrane gangliosides. *Biochim. Biophys. Acta* 1801, 868–877.
- (32) Kotler, S. A., Walsh, P., Brender, J. R., and Ramamoorthy, A. (2014) Differences between amyloid- $\beta$  aggregation in solution and on the membrane: Insights into elucidation of the mechanistic details of Alzheimer's disease. *Chem. Soc. Rev.*, DOI: 10.1039/C3CS60431D.
- (33) Jang, H., Connelly, L., Teran Arce, F., Ramachandran, S., Lal, R., Kagan, B., and Nussinov, R. (2013) Alzheimer's disease: Which type of amyloid-preventing drug agents to employ? *Phys. Chem. Chem. Phys.* 15, 8868–8877.
- (34) Jang, H., Teran Arce, F., Ramachandran, S., Kagan, B. L., Lal, R., and Nussinov, R. (2014) Disordered amyloidogenic peptides may insert into the membrane and assemble into common cyclic structural motifs. *Chem. Soc. Rev.*, DOI: 10.1039/C3CS60459D.
- (35) Williams, T. L., and Serpell, L. C. (2011) Membrane and surface interactions of Alzheimer's  $A\beta$  peptide: Insights into the mechanism of cytotoxicity. *FEBS J.* 278, 3905–3917.
- (36) Teran Arce, F., Jang, H., Connelly, L., Ramachandran, S., Kagan, B. L., Nussinov, R., and Lal, R. (2014) Structure–Function Studies of Amyloid Pores in Alzheimer's Disease as a Case Example of Neurodegenerative Diseases. In *Bio-nanoimaging: Protein Misfolding and Aggregation* (Uversky, V., and Lyubchenko, Y., Eds.) pp 397–408, Elsevier, Amsterdam.
- (37) Hallock, K. J., Lee, D.-K., and Ramamoorthy, A. (2003) MSI-78, an Analogue of the Magainin Antimicrobial Peptides, Disrupts Lipid Bilayer Structure via Positive Curvature Strain. *Biophys. J.* 84, 3052–3060.
- (38) Brender, J. R., Heyl, D. L., Samisetti, S., Kotler, S. A., Osborne, J. M., Pesaru, R. R., and Ramamoorthy, A. (2013) Membrane disordering is not sufficient for membrane permeabilization by islet amyloid polypeptide: Studies of IAPP(20–29) fragments. *Phys. Chem. Chem. Phys.* 15, 8908–8915.
- (39) Sciacca, M. F. M., Kotler, S. A., Brender, J. R., Chen, J., Lee, D. K., and Ramamoorthy, A. (2012) Two-Step Mechanism of Membrane Disruption by  $A\beta$  through Membrane Fragmentation and Pore Formation. *Biophys. J.* 103, 702–710.
- (40) Soderberg, M., Edlund, C., Alafuzoff, I., Kristensson, K., and Dallner, G. (1992) Lipid-Composition in Different Regions of the Brain in Alzheimer's Disease Senile Dementia of Alzheimer's Type. *J. Neurochem.* 59, 1646–1653.
- (41) Wells, K., Farooqui, A. A., Liss, L., and Horrocks, L. A. (1995) Neural membrane phospholipids in Alzheimer disease. *Neurochem. Res.* 20, 1329–1333.
- (42) Nielsen, L., Khurana, R., Coats, A., Frokjaer, S., Brange, J., Vyas, S., Uversky, V. N., and Fink, A. L. (2001) Effect of environmental factors on the kinetics of insulin fibril formation: Elucidation of the molecular mechanism. *Biochemistry* 40, 6036–6046.
- (43) Connelly, L., Teran Arce, F., Jang, H., Capone, R., Kotler, S. A., Ramachandran, S., Kagan, B. L., Nussinov, R., and Lal, R. (2012) Atomic Force Microscopy and MD Simulations Reveal Pore-Like Structures of All-d-Enantiomer of Alzheimer's  $\beta$ -Amyloid Peptide: Relevance to the Ion Channel Mechanism of AD Pathology. *J. Phys. Chem. B* 116, 1728–1735.
- (44) Jang, H., Teran Arce, F., Ramachandran, S., Capone, R., Azimova, R., Kagan, B. L., Nussinov, R., and Lal, R. (2010) Truncated  $\beta$ -amyloid peptide channels provide an alternative mechanism for Alzheimer's disease and Down syndrome. *Proc. Natl. Acad. Sci. U.S.A.* 107, 6538–6543.
- (45) Liu, F., Teran Arce, F., Ramachandran, S., and Lal, R. (2006) Nanomechanics of hemichannel conformations: Connexin flexibility underlying channel opening and closing. *J. Biol. Chem.* 281, 23207–23217.
- (46) Bustamante, C., Vesenka, J., Tang, C. L., Rees, W., Guthold, M., and Keller, R. (1992) Circular DNA molecules imaged in air by scanning force microscopy. *Biochemistry* 31, 22–26.
- (47) Arimon, M., Díez-Pérez, I., Kogan, M. J., Durany, N., Giralt, E., Sanz, F., and Fernández-Busquets, X. (2005) Fine structure study of  $A\beta$ 1–42 fibrillogenesis with atomic force microscopy. *FASEB J.* 19, 1344–1346.
- (48) Hutter, J. L., and Bechhoefer, J. (1993) Calibration of Atomic-Force Microscope Tips. *Rev. Sci. Instrum.* 64, 1868–1873.
- (49) Tien, H. T., Carbone, S., and Dawidowicz, E. A. (1966) Formation of "Black" Lipid Membranes by Oxidation Products of Cholesterol. *Nature* 212, 718–719.
- (50) Mueller, P., Rudin, D. O., Ti Tien, H., and Wescott, W. C. (1962) Reconstitution of Cell Membrane Structure in vitro and its Transformation into an Excitable System. *Nature* 194, 979–980.

- (51) Schlenzig, D., Manhart, S., Cinar, Y., Kleinschmidt, M., Hause, G., Willbold, D., Funke, S. A., Schilling, S., and Demuth, H.-U. (2009) Pyroglutamate Formation Influences Solubility and Amyloidogenicity of Amyloid Peptides. *Biochemistry* 48, 7072–7078.
- (52) Pifer, P. M., Yates, E. A., and Legleiter, J. (2011) Point Mutations in  $\text{A}\beta$  Result in the Formation of Distinct Polymorphic Aggregates in the Presence of Lipid Bilayers. *PLoS One* 6, e16248.
- (53) Yip, C. M., Darabie, A. A., and McLaurin, J. (2002)  $\text{A}\beta42$ -peptide assembly on lipid bilayers. *J. Mol. Biol.* 318, 97–107.
- (54) Yip, C. M., Elton, E. A., Darabie, A. A., Morrison, M. R., and McLaurin, J. (2001) Cholesterol, a modulator of membrane-associated  $\text{A}\beta$ -fibrillogenesis and neurotoxicity. *J. Mol. Biol.* 311, 723–734.
- (55) Yip, C. M., and McLaurin, J. (2001) Amyloid- $\beta$  peptide assembly: A critical step in fibrillogenesis and membrane disruption. *Biophys. J.* 80, 1359–1371.
- (56) Williams, T. L., Johnson, B. R. G., Urbanc, B., Jenkins, A. T. A., Connell, S. D. A., and Serpell, L. C. (2011)  $\text{A}\beta42$  oligomers, but not fibrils, simultaneously bind to and cause damage to ganglioside-containing lipid membranes. *Biochem. J.* 439, 67–77.
- (57) Gillman, A. L., Jang, H., Lee, J., Ramachandran, S., Kagan, B. L., Nussinov, R., and Teran Arce, F. (2014) Activity and Architecture of Pyroglutamate Modified Amyloid- $\beta$  ( $\text{A}\beta\text{pE3–42}$ ) Pores. *J. Phys. Chem. B* 118, 7335–7344.
- (58) Tosatto, L., Andrichetti, A. O., Plotegher, N., Antonini, V., Tessari, I., Ricci, L., Bubacco, L., and Serra, M. D. (2012)  $\alpha$ -Synuclein pore forming activity upon membrane association. *Biochim. Biophys. Acta* 1818, 2876–2883.
- (59) Sansom, M. S. P. (1993) Structure and Function of Channel-Forming Peptaibols. *Q. Rev. Biophys.* 26, 365–421.
- (60) Dufrene, Y. F., Barger, W. R., Green, J. B. D., and Lee, G. U. (1997) Nanometer-scale surface properties of mixed phospholipid monolayers and bilayers. *Langmuir* 13, 4779–4784.
- (61) Kunneke, S., Kruger, D., and Janshoff, A. (2004) Scrutiny of the failure of lipid membranes as a function of headgroups, chain length, and lamellarity measured by scanning force microscopy. *Biophys. J.* 86, 1545–1553.
- (62) Garcia-Manyes, S., Oncins, G., and Sanz, F. (2005) Effect of temperature on the nanomechanics of lipid bilayers studied by force spectroscopy. *Biophys. J.* 89, 4261–4274.
- (63) Garcia-Manyes, S., Oncins, G., and Sanz, F. (2005) Effect of ion-binding and chemical phospholipid structure on the nanomechanics of lipid bilayers studied by force spectroscopy. *Biophys. J.* 89, 1812–1826.
- (64) Garcia-Manyes, S., Oncins, G., and Sanz, F. (2006) Effect of pH and ionic strength on phospholipid nanomechanics and on deposition process onto hydrophilic surfaces measured by AFM. *Electrochim. Acta* 51, 5029–5036.
- (65) Nussio, M. R., Oncins, G., Ridelis, I., Szili, E., Shapter, J. G., Sanz, F., and Voelcker, N. H. (2009) Nanomechanical characterization of phospholipid bilayer islands on flat and porous substrates: a force spectroscopy study. *J. Phys. Chem. B*, 10339–10347.
- (66) Garcia-Manyes, S., Redondo-Morata, L., Oncins, G., and Sanz, F. (2010) Nanomechanics of Lipid Bilayers: Heads or Tails? *J. Am. Chem. Soc.* 132, 12874–12886.
- (67) Redondo-Morata, L., Giannotti, M. I., and Sanz, F. (2012) AFM-Based Force-Clamp Monitors Lipid Bilayer Failure Kinetics. *Langmuir* 28, 6403–6410.
- (68) Redondo-Morata, L., Oncins, G., and Sanz, F. (2012) Force Spectroscopy Reveals the Effect of Different Ions in the Nanomechanical Behavior of Phospholipid Model Membranes: The Case of Potassium Cation. *Biophys. J.* 102, 66–74.
- (69) Oncins, G., Picas, L., Hernandez-Borrell, J., Garcia-Manyes, S., and Sanz, F. (2007) Thermal response of Langmuir-Blodgett films of dipalmitoylphosphatidylcholine studied by atomic force microscopy and force spectroscopy. *Biophys. J.* 93, 2713–2725.
- (70) Cherny, I., and Gazit, E. (2008) Amyloids: Not only pathological agents but also ordered nanomaterials. *Angew. Chem., Int. Ed.* 47, 4062–4069.
- (71) Suzuki, Y., Brender, J. R., Soper, M. T., Krishnamoorthy, J., Zhou, Y., Ruotolo, B. T., Kotov, N. A., Ramamoorthy, A., and Marsh, E. N. G. (2013) Resolution of Oligomeric Species during the Aggregation of  $\text{A}\beta1–40$  Using  $^{19}\text{F}$  NMR. *Biochemistry* 52, 1903–1912.
- (72) Vivekanandan, S., Brender, J. R., Lee, S. Y., and Ramamoorthy, A. (2011) A partially folded structure of amyloid- $\beta$ (1–40) in an aqueous environment. *Biochem. Biophys. Res. Commun.* 411, 312–316.
- (73) Kayed, R., Pensalfini, A., Margol, L., Sokolov, Y., Sarsoza, F., Head, E., Hall, J., and Glabe, C. (2009) Annular Protofibrils Are a Structurally and Functionally Distinct Type of Amyloid Oligomer. *J. Biol. Chem.* 284, 4230–4237.
- (74) Conway, K. A., Harper, J. D., and Lansbury, P. T. (2000) Fibrils Formed in Vitro from  $\alpha$ -Synuclein and Two Mutant Forms Linked to Parkinson's Disease are Typical Amyloid. *Biochemistry* 39, 2552–2563.
- (75) Janson, J., Ashley, R. H., Harrison, D., McIntyre, S., and Butler, P. C. (1999) The mechanism of islet amyloid polypeptide toxicity is membrane disruption by intermediate-sized toxic amyloid particles. *Diabetes* 48, 491–498.
- (76) Arispe, N., Pollard, H. B., and Rojas, E. (1993) Giant multilevel cation channels formed by Alzheimer disease amyloid  $\beta$ -protein [ $\text{A}\beta\text{P}(1–40)$ ] in bilayer membranes. *Proc. Natl. Acad. Sci. U.S.A.* 90, 10573–10577.
- (77) Arispe, N., Rojas, E., and Pollard, H. B. (1993) Alzheimer disease amyloid  $\beta$  protein forms calcium channels in bilayer membranes: Blockade by tromethamine and aluminum. *Proc. Natl. Acad. Sci. U.S.A.* 90, 567–571.
- (78) Connelly, L., Jang, H., Teran Arce, F., Ramachandran, S., Kagan, B. L., Nussinov, R., and Lal, R. (2012) Effects of Point Substitutions on the Structure of Toxic Alzheimer's  $\beta$ -Amyloid Channels: Atomic Force Microscopy and Molecular Dynamics Simulations. *Biochemistry* 51, 3031–3038.
- (79) Mustata, M., Capone, R., Jang, H., Teran Arce, F., Ramachandran, S., Lal, R., and Nussinov, R. (2009) K3 Fragment of Amyloidogenic  $\beta_2$ -Microglobulin Forms Ion Channels: Implication for Dialysis Related Amyloidosis. *J. Am. Chem. Soc.* 131, 14938–14945.
- (80) Brulet, P., and McConnell, H. M. (1976) Lateral Hapten Mobility and Immunochemistry of Model Membranes. *Proc. Natl. Acad. Sci. U.S.A.* 73, 2977–2981.
- (81) Byfield, F. J., Aranda-Espinoza, H., Romanenko, V. G., Rothblat, G. H., and Levitan, I. (2004) Cholesterol depletion increases membrane stiffness of aortic endothelial cells. *Biophys. J.* 87, 3336–3343.
- (82) Demel, R. A., and Dekruyff, B. (1976) Function of Sterols in Membranes. *Biochim. Biophys. Acta* 457, 109–132.
- (83) Evans, E., and Needham, D. (1987) Physical Properties of Surfactant Bilayer-Membranes: Thermal Transitions, Elasticity, Rigidity, Cohesion, and Colloidal Interactions. *J. Phys. Chem.* 91, 4219–4228.
- (84) Needham, D., and Nunn, R. S. (1990) Elastic-Deformation and Failure of Lipid Bilayer-Membranes Containing Cholesterol. *Biophys. J.* 58, 997–1009.
- (85) Redondo-Morata, L., Giannotti, M. I., and Sanz, F. (2012) Influence of Cholesterol on the Phase Transition of Lipid Bilayers: A Temperature-Controlled Force Spectroscopy Study. *Langmuir* 28, 12851–12860.
- (86) Stockton, G. W., and Smith, I. C. P. (1976) Deuterium Nuclear Magnetic-Resonance Study of Condensing Effect of Cholesterol on Egg Phosphatidylcholine Bilayer Membranes. 1. Perdeuterated Fatty-Acid Probes. *Chem. Phys. Lipids* 17, 251–263.
- (87) Xu, X. L., and London, E. (2000) The effect of sterol structure on membrane lipid domains reveals how cholesterol can induce lipid domain formation. *Biochemistry* 39, 843–849.
- (88) Canale, C., Seghezza, S., Vilasi, S., Carrotta, R., Bulone, D., Diaspro, A., Biagio, P. L. S., and Dante, S. (2013) Different effects of Alzheimer's peptide  $\text{A}\beta(1–40)$  oligomers and fibrils on supported lipid membranes. *Biophys. Chem.* 182, 23–29.
- (89) Dante, S., Hauss, T., Steitz, R., Canale, C., and Dencher, N. A. (2011) Nanoscale structural and mechanical effects of  $\beta$ -amyloid (1–42) on polymer cushioned membranes: A combined study by neutron reflectometry and AFM force spectroscopy. *Biochim. Biophys. Acta* 1808, 2646–2655.

- (90) Jang, H., Teran Arce, F., Ramachandran, S., Kagan, B. L., Lal, R., and Nussinov, R. (2013) Familial Alzheimer's disease Osaka mutant ( $\Delta E22$ )  $\beta$ -barrels suggest an explanation for the different  $A\beta 1-40/42$  preferred conformational states observed by experiment. *J. Phys. Chem. B* 117, 11518–11529.
- (91) Jang, H., Zheng, J., and Nussinov, R. (2007) Models of  $\beta$ -Amyloid Ion Channels in the Membrane Suggest That Channel Formation in the Bilayer Is a Dynamic Process. *Biophys. J.* 93, 1938–1949.
- (92) Jang, H., Teran Arce, F., Ramachandran, S., Capone, R., Lal, R., and Nussinov, R. (2010) Structural convergence among diverse, toxic  $\beta$ -sheet ion channels. *J. Phys. Chem. B* 114, 9445–9451.
- (93) Jang, H., Teran Arce, F., Ramachandran, S., Capone, R., Lal, R., and Nussinov, R. (2010)  $\beta$ -Barrel Topology of Alzheimer's  $\beta$ -Amyloid Ion Channels. *J. Mol. Biol.* 404, 917–934.